Journal of Materials Science: Materials in Electronics (2018) 29:5134–5142
https://doi.org/10.1007/s10854-017-8477-y

Conduction mechanism and magnetic behavior of Cu doped barium hexaferrite ceramics

Muhammad Asif Rafiq[1] · Moaz Waqar[1] · Qaisar Khushi Muhammad[1,3] · Masam Waleed[1] · Murtaza Saleem[2] · Muhammad Sabieh Anwar[2]

Received: 9 September 2017 / Accepted: 22 December 2017 / Published online: 28 December 2017

Abstract
M-type barium hexaferrite ceramics (BaM) are important materials owing to their tremendous applications and useful properties. However magnetic and electrical properties of Cu substituted BaM haven't been studied yet. In the present study, Cu doped BaM samples having chemical formula $BaFe_{12-x}Cu_xO_{19}$ (where x = 0, 0.1, 0.3 and 0.5) were synthesized by conventional solid state mixed oxide route. X-ray diffraction and Fourier transform infrared spectroscopy confirmed the formation of hexagonal magnetoplumbite structure with space group *P63/mmc* as the major phase in all the samples. Scanning electron microscopy revealed the dense structure of undoped and doped samples with platelet-like morphology. Vibrating sample magnetometry showed a large decrease in the coercivity of BaM without the loss of saturation magnetization by the addition of Cu. Magnetic measurement at cryogenic temperature (25 K) revealed that Cu doped sample showed less variation in magnetic properties on decreasing the temperature as compared to undoped BaM samples. Room temperature dielectric studies showed that addition of Cu caused a decrease in dielectric loss however it increased at higher substitution level i.e. x = 0.5. High temperature conductivity studies revealed that single-ionized oxygen vacancies are responsible for conduction in Cu doped BaM.

1 Introduction

Hexagonal ferrites are complex oxides of iron (Fe) with various other divalent metal ions chemically combined in different ratios and categorized as M, W, X, Y, Z and U type hexaferrites [1]. These materials have become very important for last few decades both technologically and commercially owing to their multitude of applications in magnetic recording devices, loudspeakers, small direct current (DC) motors, electric power generation, ferrite cores, sensors, transistors, capacitors, inductors, microwave absorbers and microelectromechanical systems (MEMS) [1–5]. Among all other types of hexaferrites, M-type hexaferrites specially barium hexaferrite ($BaFe_{12}O_{19}$, BaM) has gained tremendous attention of researchers due to its useful properties including relatively large saturation magnetization (72 $Am^2\ kg^{-1}$), high magnetocrystalline anisotropy along c axis (1352 kAm^{-1}), large coercivity (594 kAm^{-1}), high Curie temperature (450 °C), chemical stability, low cost, ability to resist corrosion, high electrical resistivity and low dielectric losses [1, 3–9]. High coercivity of BaM is attributed to its large c/a ratio (3.94) and high anisotropy constant ($K_1 = 3.3 \times 10^6$ erg cm^{-3}) which renders its various applications as hard magnets. However, the coercivity (H_c) and other magnetic properties of BaM can be altered by substituting Fe with various other dopants or/and by using different synthesis techniques to broaden the span of its commercial applications while retaining its useful properties including chemical stability and high electrical resistivity [1].

BaM, having space group *P63/mmc*, consists of Fe^{3+} ions randomly distributed in tetrahedral ($4f_1$), octahedral (12k, $4f_2$, 2a) and trigonal bipyramidal (2b) sites in alternating

✉ Muhammad Asif Rafiq
asifrafiq@uet.edu.pk

[1] Department of Metallurgical and Materials Engineering, University of Engineering and Technology, G.T. Road, Lahore 54890, Pakistan

[2] Department of Physics, Syed Babar Ali School of Science and Engineering, Lahore University of Management Sciences (LUMS), Opposite Sector U, D.H.A., Lahore 54792, Pakistan

[3] Present Address: Pakistan Institute of Technology for Minerals and Advanced Engineering Materials (PITMAEM), Pakistan Council of Scientific & Industrial Research (PCSIR), Laboratories Complex, Lahore 54600, Pakistan

hexagonally and cubically packed layers of Ba and O. Net magnetic polarization (J) at any temperature T per unit formula of BaM can be given by [3, 10].

$$J(T) = 6m_{12k}(T) - 2m_{4f1}(T) - 2m_{4f2}(T) + 1m_{2a}(T) + 1m_{2b}(T) \quad (1)$$

where m_n is the magnetic moment of Fe^{3+} ions in the nth sub-lattice. It has also been reported that Fe^{3+} ion at 2b site has the largest contribution to K_1, while ions at the 2a, $4f_1$, and $4f_2$ sites have relatively smaller effect. Contrarily, Fe^{3+} ion at 12k has a negative contribution to the anisotropy constant. Hence, the choice of an appropriate ion for the replacement of Fe ions in BaM can be helpful in controlling its magnetic properties for the growth of its commercial applications.

Researchers have replaced Fe with various trivalent ions (Ce^{3+} [11], Al^{3+} [8], Cr^{3+} [12], Sm^{3+} [7], Ho^{3+} [9], Ga^{3+} [13]) and a combination of divalent and tetravalent ions (Mg^{2+}–Ti^{2+} [5], Ni^{2+}–Sn^{4+} [10], Cu^{2+}–Ti^{4+} [10], Ni^{2+}–Zr^{4+} [14]). It was found that replacing Fe with Ce^{3+}, Sm^{3+}, Ho^{3+} and Ga^{3+} caused an increase in coercivity while Al^{3+}, Cr^{3+}, Mg^{2+}–Ti^{2+}, Ni^{2+}–Sn^{4+}, Cu^{2+}–Ti^{4+} and Ni^{2+}–Zr^{4+} caused a decrease in the coercivity of BaM. Saturation magnetization (M_s) and remanent magnetization (M_r) decreased in all the above reported cases. Scientists have also used various synthesis routes including solid state oxide route [3], hydrothermal method [15], glass crystallization method [16], microemulsion [17], co-precipitation [18], citrate precursor [19] and sol–gel auto-combustion method [20] to produce BaM with wide range of coercivity. Solid state oxide route yields powder well below single-domain grain size and uses simple equipment and synthesis methodology [3].

Cu^{2+} ions are believed to behave in the similar way as Co^{2+} ions [21] and it is already known that addition of Co^{2+} decreases the coercivity of BaM due to its negative first order magnetocrystalline anisotropy constant [22]. Sözeri et al. [10] doped BaM with Cu^{2+} in combination with Ti and reported a decrease in coercivity without having much effect on its saturation magnetization. However, a detailed investigation on the effect of solely Cu on polycrystalline BaM ceramics is still scarce in literature. In present work, the effect of Cu on the structural, magnetic and electrical properties of BaM has been investigated using advanced analytical tools. X-ray diffraction (XRD) and Fourier transform infrared spectroscopy (FTIR) has been used to investigate the structural changes. Grain size and morphological aspects have been studied by scanning electron microscopy (SEM) analysis. Vibrating sample magnetometer (VSM) was used to determine the magnetic properties both at room and cryogenic temperatures. Impedance analysis is an important modern tool to characterize the electrical properties of ceramics since an increasing interest has been developed among researchers to evaluate the dielectric response of BaM for the purpose of advanced electronic applications [1, 10, 23–25]. Therefore a detailed dielectric study has been done to investigate the dielectric properties, conduction mechanism and the activation energy of samples using precision impedance analyzer.

2 Experimental procedure

Cu doped BaM samples having chemical formula $BaFe_{12-x}Cu_xO_{19}$ (where x = 0, 0.1, 0.3 and 0.5) were synthesized by conventional solid state mixed oxide route. Stoichiometric amounts of dried $BaCO_3$ (Riadel-de Haen, 99%), Fe_2O_3 (UniChem, 99.5%) and CuO (Grey/Green British House Drug Ltd., 99%) powders were carefully weighed and milled in ethyl alcohol for 4 h. After milling, the resultant powder was heated to 900 °C at a rate of 20 °C min^{-1} and calcined for 5 h in air atmosphere. Calcined powder was further ground in ball mill using ethyl alcohol as solvent for 3 h and was converted into 10×1 mm^2 cylindrical pellets using uniaxial hydraulic press. Phase and crystallographic studies were done using X-ray diffractometer (PANalytical Xpert PRO) with Cu–Kα (λ = 0.154 nm) radiation. Morphology and particle size of the samples were analyzed using scanning electron microscope (Nova NanoSEM-450). Infrared spectroscopic analysis was done by using FTIR (Jasco FT/IR-4100) spectrometer. Magnetic measurements of samples were done at cryogenic (25 K) and room temperature by using vibrating sample magnetometer [Model: 7407, Lakeshore (USA)]. Precision impedance analyzer (Wayne kerr 6500B) was used to determine room temperature dielectric properties and high temperature conductivity (upto 210 °C) in the frequency range of 1 kHz–2 MHz.

3 Results and discussion

3.1 X-ray diffraction

The XRD patterns of $BaFe_{12-x}Cu_xO_{19}$ (x = 0, 0.1, 0.3 and 0.5) powders sintered at 1300 °C for 2 h in air are shown in Fig. 1. XRD patterns confirmed the formation of $BaFe_{12}O_{19}$ as a major phase in all the prepared samples. However, $BaFeO_{3-\delta}$ appeared as an impurity in the undoped sample. It is already known from the literature that formation of single phase $BaFe_{12}O_{19}$ is very difficult via both conventional solid state and wet methods [1, 19, 26]. It was observed that addition of Cu suppressed the formation of impurity phase in samples $BaFe_{11.9}Cu_{0.1}O_{19}$ and $BaFe_{11.7}Cu_{0.3}O_{19}$. This type of behavior in which a dopant promotes the sintering process and restricts the formation of impurity phase, has been reported in several other cases [3, 27]. However, hematite (Fe_2O_3) appeared as an impurity at higher substitution level

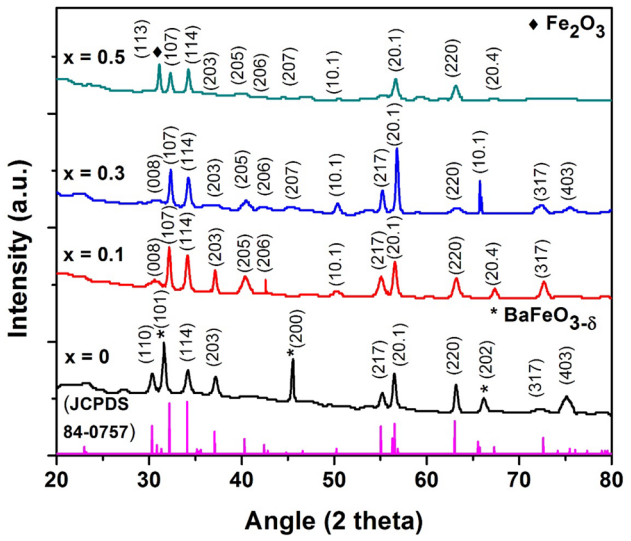

Fig. 1 XRD patterns for $BaFe_{12-x}Cu_xO_{19}$ for different values of x. Hexagonal magnetoplumbite structure (space group: *P63/mmc*) was formed in all the samples as a major phase

i.e. x = 0.5. All the peaks were indexed in accordance with Joint Committee on Powder Diffraction Standards (JCPDS) no. 84-0757 for $BaFe_{12}O_{19}$, 23-1023 for $BaFeO_{3-\delta}$ and 40-1139 for Fe_2O_3. Standard pattern of $BaFe_{12}O_{19}$ has also been displayed at the base of Fig. 1 for quick reference.

Lattice parameters a and c were calculated according to the formula [13].

$$\frac{1}{d_{hkl}^2} = \frac{4\left(h^2 + hk + k^2\right)}{3a^2} + \frac{l^2}{c^2} \tag{2}$$

In the given equation, d is interplanar spacing as determined by the Bragg formula $2d\sin\theta = n\lambda$. The unit cell volume was calculated from the formula [13].

$$V_{cell} = \frac{\sqrt{3}}{2}a^2c \tag{3}$$

Table 1 shows the effect of Cu doping on the lattice parameters of BaM. The lattice constants of pure BaM are in good agreement with the previous work [1]. It is evident from Table 1 that the lattice parameter 'c' increased upto x = 0.1 but started decreasing afterwards. The increase in 'c' can be explained on the basis of larger ionic radius of Cu^{2+} ions ($r(Cu^{2+}) = 0.57$ Å for CN = 4 and $r(Cu^{2+}) = 0.73$ Å for CN = 6 [28]) which are replacing smaller Fe^{3+} ions ($r(Fe^{3+}) = 0.49$ for CN = 4 and $r(Fe^{3+}) = 0.65$ Å for CN = 6 [28]) in the hexagonal crystal lattice [29]. At higher substitution rates, apparently the formation of oxygen vacancies (to balance the charge as divalent ions are being replaced by trivalent ions) has a greater effect on lattice parameters as compared to the substitution of Fe^{3+} ions by Cu^{2+} ions in the unit cell, which consequently results in the decrease in lattice parameters [3, 30].

Table 1 Values of lattice constants 'a' and 'c', c/a ration and volume of unit cell of $BaFe_{12-x}Cu_xO_{19}$

Composition	a (Å)	c (Å)	c/a	V_{cell}
$BaFe_{12}O_{19}$	5.89	23.11	3.93	693.21
$BaFe_{11.9}Cu_{0.1}O_{19}$	5.89	23.15	3.93	695.14
$BaFe_{11.7}Cu_{0.3}O_{19}$	5.88	23.06	3.93	689.23
$BaFe_{11.5}Cu_{0.5}O_{19}$	5.89	22.86	3.88	685.91

3.2 Fourier transformed infrared spectroscopy

Figure 2 shows the IR spectra recorded for $BaFe_{12-x}Cu_xO_{19}$ (where x = 0, 0.1, 0.3 and 0.5) ceramics. Two absorption peaks can be observed in the range of 400–600 cm^{-1} which can be related to the characteristic vibration band of hexagonal ferrite [4, 31]. Band in the range 420–470 cm^{-1} can be assigned to Fe–O bending by Fe–O_4 and Fe–O stretching by Fe–O_6 whereas, the band in the range 520–550 cm^{-1} can be assigned to the Fe–O stretching by Fe–O_4 [4, 31, 32]. The positions of all absorption bands of the products are very similar, while their relative intensities varied slightly. The absorption peak in the range of 630–640 cm^{-1} present in all the samples can be attributed to the metal–oxygen stretching vibrations of Fe_2O_3 [33].

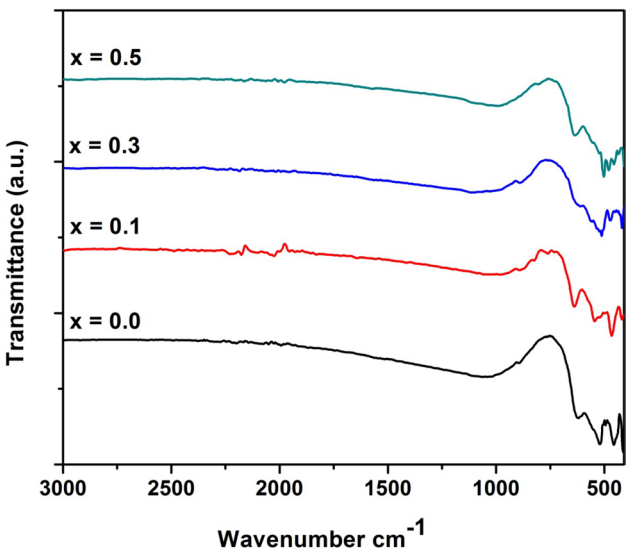

Fig. 2 FTIR spectra of $BaFe_{12-x}Cu_xO_{19}$ for x = 0, 0.1, 0.3 and 0.5

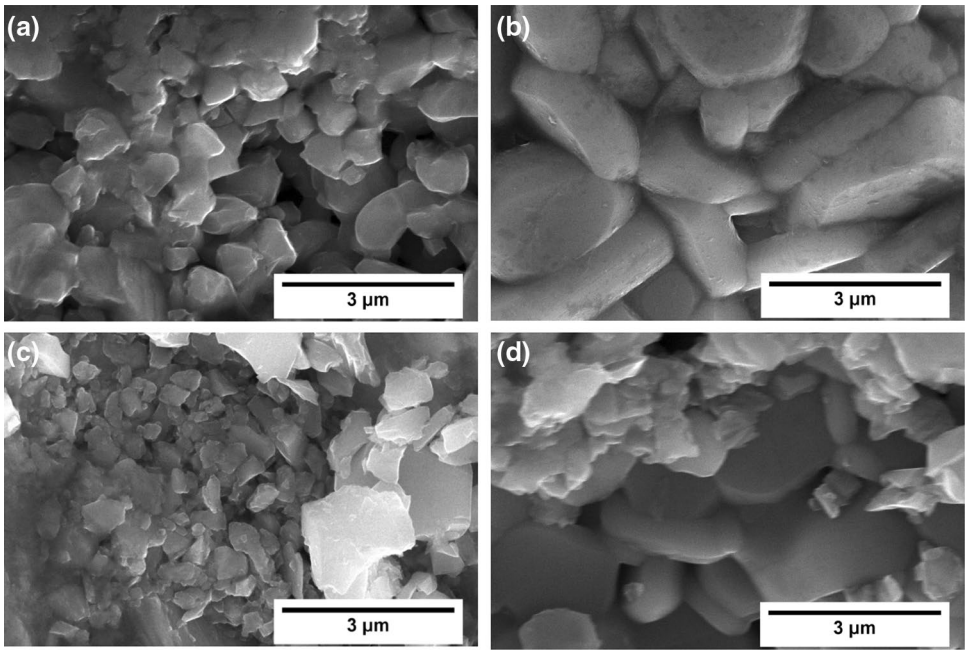

Fig. 3 SEM images of **a** $BaFe_{12}O_{19}$, **b** $BaFe_{11.9}Cu_{0.1}O_{19}$, **c** $BaFe_{11.7}Cu_{0.3}O_{19}$ and **d** $BaFe_{11.5}Cu_{0.5}O_{19}$

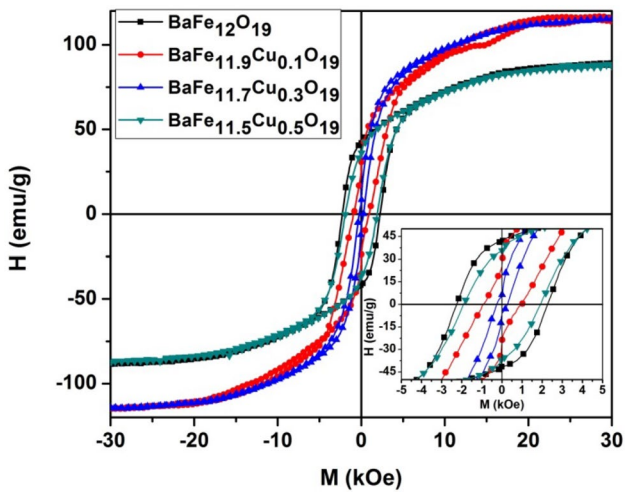

Fig. 4 M–H loops for $BaFe_{12-x}Cu_xO_{19}$ ceramics for x = 0, 0.1, 0.3 and 0.5

3.3 Scanning electron microscopy

Microstructural analysis of fractured surface of Cu doped BaM ceramic samples was done using SEM and the resulting micrographs have been shown in Fig. 3. Dense microstructure with platelet-like morphology can be observed in Fig. 3a–d, which is in accordance with XRD analysis.

3.4 Magnetic properties

Figure 4 represents the hysteresis loops of $BaFe_{12-x}Cu_xO_{19}$ (where x = 0, 0.1, 0.3 and 0.5) ceramics measured at a maximum applied field of 18 kOe at room temperature. The values of saturation magnetization (M_s), remanent magnetization (M_r) and coercive force (H_c) measured for all samples are given in Table 2. It can be observed that M_s increased from 89 to 115.0 emu g^{-1} with the addition of Cu to x = 0.3 in undoped sample and then it decreased to 88.5 emu g^{-1} on further addition of Cu to x = 0.5. The increase in M_s of BaM by the addition of Cu can be explained by Ligand field theory; according to this, ions with d^1, d^2, d^3 and d^4 electrons prefer tetrahedral coordination, while ions with d^6, d^7, d^8 and d^9 electrons prefer octahedral coordination [3, 34, 35]. Therefore Cu^{2+} ions, which have d^9 electrons, are expected to replace Fe^{3+} ions at $4f_2$ site which is octahedrally coordinated position having spin down moment. According to Eq. 1, substitution of Fe^{3+} ions (with magnetic moment of 5 μ_B/ion) at $4f_2$ position by Cu^{2+} ions (having lesser magnetic moment) should lead to an increase in the net magnetic polarization (J) of BaM which can account for the initial increase in the M_s. The decrease in M_s afterwards can be explained by the fact that at higher substitution level, large increase in c-axis length decreases the effect of down-spin state contributions ($4f_2$) to the total magnetization [36].

Table 2 Effect of dopant on magnetic properties of $BaFe_{12-x}Cu_xO_{19}$ ceramics for x = 0, 0.1, 0.3 and 0.5

x	Saturation magnetization M_s (emu g^{-1})	Remanent magnetization M_r (emu g^{-1})	Coercivity H_c (Oe)
0	89.0	41.3	2263.1
0.1	115.0	25.9	932.5
0.3	115.1	5.9	262.1
0.5	88.5	35.4	1911.0

As evident from Table 2, both M_r and H_c decreased with increase in Cu content upto x = 0.3 and then increased at x = 0.5. A high H_c value for pure BaM is attributed to its high uniaxial anisotropy along the c-axis [1]. In M-type hexaferrites the ions at octahedral coordination sites (12k, $4f_2$) and 2b (trigonal bi-pyramidal coordination) sites are known to be the major contributors to the magneto crystalline anisotropy. Large decrease in H_c can be related to the reduction of the anisotropy field as a result of Cu^{2+} substitution at $4f_2$ site, which provides the largest contribution to magnetocrystalline anisotropy [10, 36–38]. Increase in H_c at higher dopant concentration can be attributed to the weakening of super exchange interactions. An excessive amount of Cu^{2+} ions might destroy the regular arrangement of Fe^{3+} ions, which would lead to an increase in H_c [11]. More specifically large substitution causes weakening of super exchange interaction of type FeA^{3+}–O–FeB^{3+}, leading to the collapse of magnetic collinearity of the lattice [8].

Figure 5 shows the variation in magnetic properties of BaM due to the drop in temperature to 25 K for undoped and doped samples. It is evident that addition of Cu has diminished the effect of cryogenic temperature on the magnetic properties of BaM.

3.5 Dielectric studies

Dielectric characteristics of $BaFe_{12-x}Cu_xO_{19}$ (where x = 0, 0.1, 0.3 and 0.5) were measured over frequency range of 1 kHz–2 MHz at ambient temperature and the results are shown in Fig. 6. The variation of real and imaginary part of complex permittivity (ε′ and ε″) with frequency is shown in Fig. 6a, b. The real part of the complex permittivity (ε′) represents the quantity of energy stored in the dielectric material from the alternating current (AC) field and imaginary part (ε″) represents the losses [4]. The real and imaginary part of permittivity (ε′, ε″) decreased with increasing frequency for all the compositions and this trend can be explained using the correlation of frequency and polarization. The total or net polarization of a dielectric material is the sum of contributions from ionic, electronic, dipolar and interfacial polarizations [23, 24, 39, 40]. These polarizations are quite responsive to the time varying electric field at low frequency, but as the frequency of electric field is increased, the contributions from different polarization filter out one by one which results in the decrease of net polarization. Hence, permittivity of the ceramics generally decreases with increasing frequency [24, 39, 41]. Also, ferrites are characterized by conducting grains and highly resistive grain boundaries. When they are subjected to electric field, charge carriers start traveling towards the grain boundary (GB) through hopping phenomenon and then start piling up due to the high resistance of the GB. This piling of

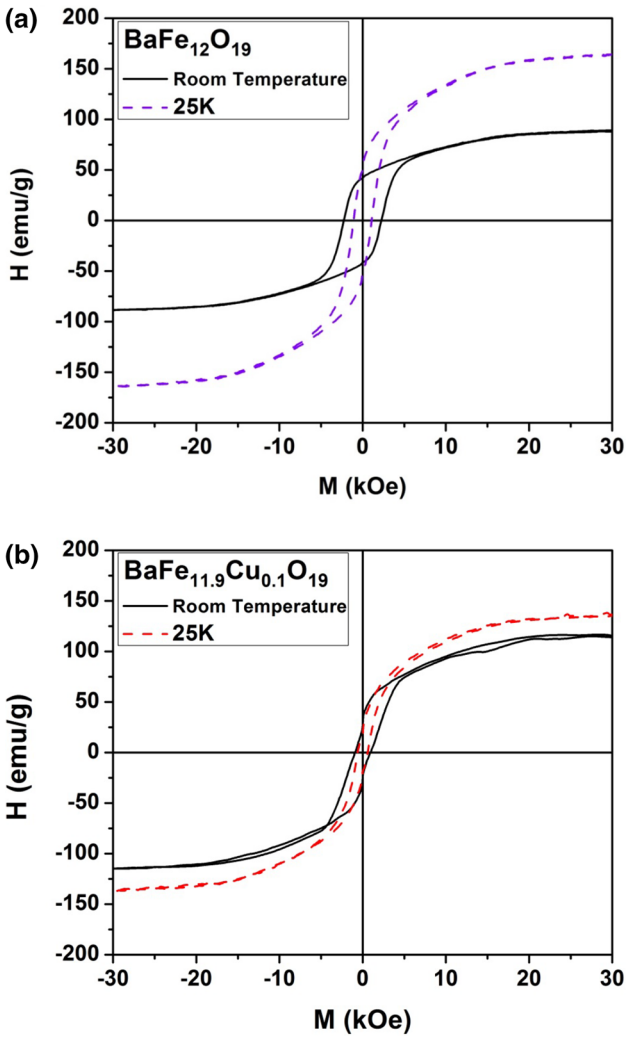

Fig. 5 Variation in magnetic properties of BaM due to the drop in temperature to 25 K for **a** undoped and **b** doped (x = 0.1) samples

charges causes polarization and when the frequency of the applied electric field is increased, the charges tend to reverse the direction of their motion more often. This phenomenon decreases the probability of electrons to reach the GB and as a result the polarization decreases. Consequently, the dielectric constant starts decreasing with increasing frequency of the applied electric field. The results obtained in the present work are in accordance with precious reports [23, 24, 42]. It can also be seen in Fig. 6a, b that the real part of permittivity (ε′) and imaginary part (ε″) increased with the increase in Cu^{2+} except for $BaFe_{11.9}Cu_{0.1}O_{19}$. Figure 6c indicates the variation of dielectric loss (tan δ) with increasing frequency for various amounts of Cu (x = 0, 0.1, 0.3 and 0.5). The value of dielectric loss varied between 0.01 and 0.14 for all the compositions at lower frequency. Further decrease in dielectric loss was observed with the increase

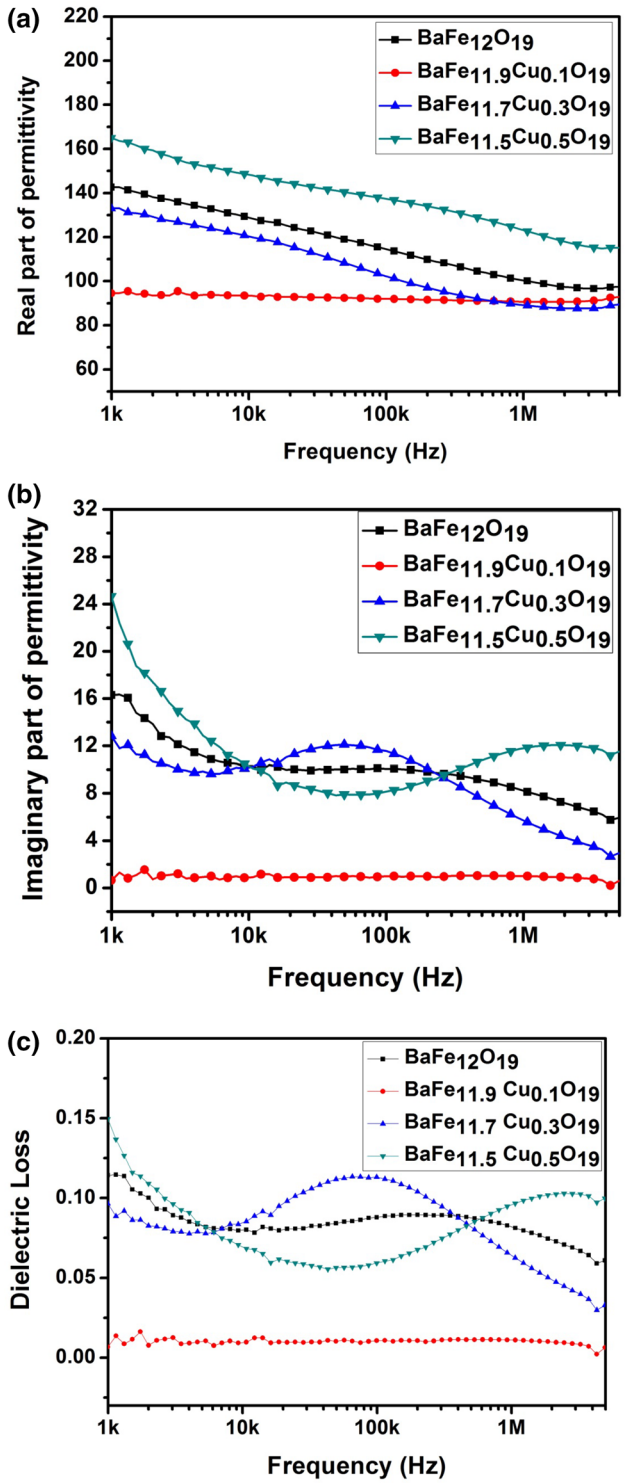

Fig. 6 Effect of frequency on **a** Real part of permittivity, **b** Imaginary part of permittivity and **c** Dielectric loss of $BaFe_{12-x}Cu_xO_{19}$ for x = 0, 0.1, 0.3 and 0.5

in frequency. This decrease can probably be due to the fact that the dipole oscillations cannot follow the changes of the external field at high frequencies [43].

3.6 Conductivity analysis

Figure 7 shows the AC-conductivity (σ_{ac}) as a function of frequency in temperature range of 30–210 °C. AC conductivity (σ_{ac}) of all the samples was quantified via impedance analysis by using relation [44],

$$\sigma = \frac{Z'}{Z'^2 + Z''^2} \times \frac{t}{A} \tag{4}$$

where Z′ and Z″ are real and imaginary part of impedance and (*t*/*A*) are dimensions of sample. It is very clear that with the rise in temperature AC-conductivity increases. This rise in AC-conductivity can be divided into two regions. A small increase in AC-conductivity was observed up to 130 °C and it increased to a large extent from 130 to 210 °C. As far as frequency dependence of AC-conductivity is concerned, at lower frequencies plot showed narrow dispersion which turned out to be wider after 100 kHz. This step like feature in Z′ (ω) and σ_{ac} (ω) with rise in temperature is an indication of multiple potentials countered by charge carriers near GB and electrode surface as the formula unit contains 12 no. of iron atoms [45, 46].

AC-conductivity behavior with temperature for $BaFe_{11.9}Cu_{0.1}O_{19}$ is shown in Fig. 8. The plot could be distributed, independent of frequency, in two regions categorized by different slopes. At low temperature (region-I), frequency dependence is high as all conductivity curves are wide spread. While at high temperature (region-II) these curves are merging together. Each region is characterized by different slopes which indicates diverse conduction mechanisms associated with the corresponding values of activation energy (E_a). Moreover, the AC conductivity increases with measuring frequencies especially at high temperatures. As the temperature increases, the conductivity becomes frequency independent with a slight increase on the higher frequency side. Similar trend is shown by all other compositions. In order to explain the conduction mechanism at different frequencies, activation energies are calculated by employing Arrhenius relation [27, 47],

$$\tau = \tau_o \exp\left(E_a/k_B T\right) \tag{5}$$

where τ_o is the pre-exponential factor, E_a is the associated activation energy and k_B stands for Boltzmann constant (1.3807×10^{-23} J K^{-1}). Activation energy values for all the sintered samples at different frequencies are calculated and presented in Table 3.

Activation energy values are found to decrease at higher frequencies. It has been reported in the literature that activation energy is in the range of 0.3–0.6 eV and 0.6–1.2 eV for single-ionized and doubly ionized oxygen vacancies respectively [48]. Taking this into account, conduction

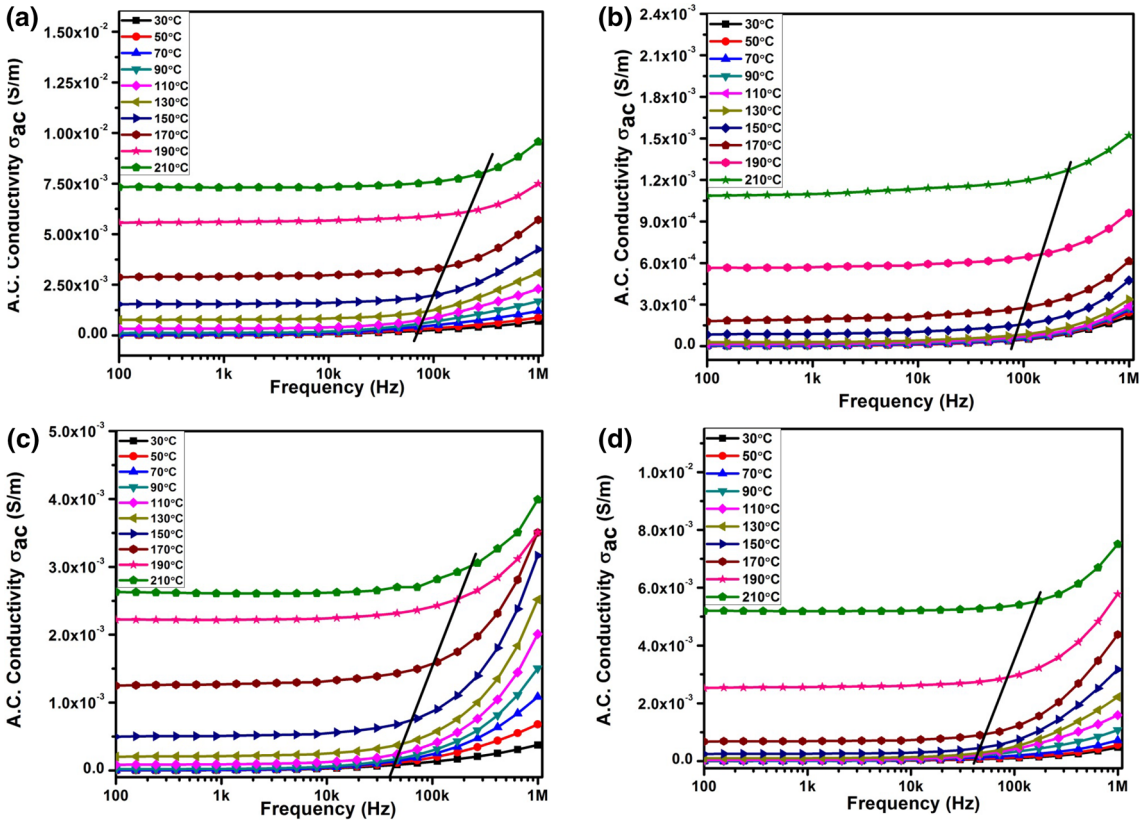

Fig. 7 Frequency dependence of AC-conductivity for **a** $BaFe_{12}O_{19}$, **b** $BaFe_{11.9}Cu_{0.1}O_{19}$, **c** $BaFe_{11.7}Cu_{0.3}O_{19}$ and **d** $BaFe_{11.5}Cu_{0.5}O_{19}$ at temperature ranging from 30 to 210 °C

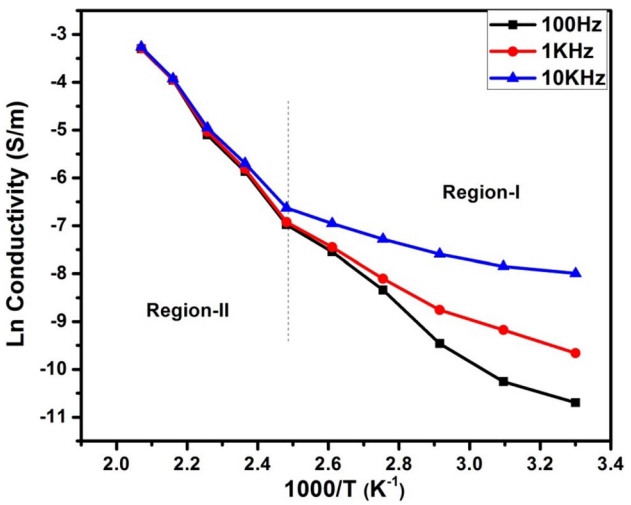

Fig. 8 Plot of AC conductivity (ln-scale) vs. temperature for $BaFe_{11.9}Cu_{0.1}O_{19}$ from 30 to 210 °C at different frequencies

mechanism in $BaFe_{12-x}Cu_xO_{19}$ is due to conduction of single-ionized oxygen vacancies.

Table 3 Activation energy values (eV) at different frequencies in temperature range of 30–210 °C

Composition	Activation energy (eV)		
	100 Hz	1 kHz	10 kHz
$BaFe_{12}O_{19}$	0.52	0.48	0.37
$BaFe_{11.9}Cu_{0.1}O_{19}$	0.53	0.45	0.33
$BaFe_{11.7}Cu_{0.3}O_{19}$	0.59	0.49	0.35
$BaFe_{11.5}Cu_{0.5}O_{19}$	0.64	0.54	0.38

4 Conclusion

Cu doped BaM samples having composition $BaFe_{12-x}Cu_xO_{19}$ (where x = 0, 0.1, 0.3 and 0.5) were successfully synthesized by conventional solid state mixed oxide route. XRD and FTIR spectroscopy confirmed the formation of hexagonal magnetoplumbite structure with space group *P63/mmc* as the major phase in all the samples. $BaFeO_{3-\delta}$ appeared as a secondary phase in undoped sample which was eliminated by the addition of Cu. SEM revealed dense platelet-like structure of samples. Addition of Cu caused a large decrease in coercivity of BaM from 2263.1 to 262.1 Oe at x = 0.3

while retaining a high value of M_s i.e. 115.1 emu g^{-1}. Magnetic measurement at cryogenic temperature (25 K) revealed that Cu doped sample showed less variation in magnetic properties on decreasing the temperature as compared to undoped BaM samples. Room temperature dielectric studies showed that addition of Cu caused a decrease in dielectric loss from 0.11 to 0.01 at x = 0.1 which started increasing afterwards at higher substitution level. High temperature conductivity studies revealed that single-ionized oxygen vacancies are responsible for conduction in Cu doped BaM. $BaFe_{11.7}Cu_{0.3}O_{19}$ ceramics showed lowest value of coercivity (H_c) i.e. 262.1 Oe while having highest value of saturation magnetization i.e. 115.1 emu g^{-1} hence these ceramics are quite suitable for switching device applications.

Compliance with ethical standards

Conflict of interest The authors declare that they have no conflict of interest.

References

1. R.C. Pullar, Hexagonal ferrites: a review of the synthesis, properties and applications of hexaferrite ceramics. Prog. Mater. Sci. **57**(7), 1191–1334 (2012)
2. V. Anbarasu et al., Effect of divalent cation substitution in the magnetoplumbite structured $BaFe_{12}O_{19}$ system. J. Mater. Sci.: Mater. Electron. **24**(3), 916–926 (2013)
3. M.A. Rafiq et al., Effect of Ni^{2+} substitution on the structural, magnetic, and dielectric properties of barium hexagonal ferrites ($BaFe_{12}O_{19}$). J. Electron. Mater. **46**(1), 241–246 (2017)
4. Z. Mosleh et al., Structural, magnetic and microwave absorption properties of Ce-doped barium hexaferrite. J. Magn. Magn. Mater. **397**, 101–107 (2016)
5. M.H. Shams et al., Effect of Mg^{2+} and Ti^{4+} dopants on the structural, magnetic and high-frequency ferromagnetic properties of barium hexaferrite. J. Magn. Magn. Mater. **399**, 10–18 (2016)
6. M.S.E. Shafie et al., Magnetic M–H loops family characteristics in the microstructure evolution of $BaFe_{12}O_{19}$. J. Mater. Sci.: Mater. Electron. **25**(9), 3787–3794 (2014)
7. L. Wang et al., XAFS and XPS studies on site occupation of Sm^{3+} ions in Sm doped M-type $BaFe_{12}O_{19}$. J. Magn. Magn. Mater. **377**, 362–367 (2015)
8. V.N. Dhage et al., Structural and magnetic behaviour of aluminium doped barium hexaferrite nanoparticles synthesized by solution combustion technique. Phys B **406**(4), 789–793 (2011)
9. G.M. Rai, M. Iqbal, K. Kubra, Effect of Ho^{3+} substitutions on the structural and magnetic properties of $BaFe_{12}O_{19}$ hexaferrites. J. Alloy. Compd. **495**(1), 229–233 (2010)
10. H. Sözeri et al., Magnetic, dielectric and microwave properties of M–Ti substituted barium hexaferrites (M = Mn^{2+}, Co^{2+}, Cu^{2+}, Ni^{2+}, Zn^{2+}). Ceram. Int. **40**(6), 8645–8657 (2014)
11. R.A. Pawar et al., Ce^{3+} incorporated structural and magnetic properties of M type barium hexaferrites. J. Magn. Magn. Mater. **378**, 59–63 (2015)
12. V.N. Dhage et al., Influence of chromium substitution on structural and magnetic properties of $BaFe_{12}O_{19}$ powder prepared by sol–gel auto combustion method. J. Alloy. Compd. **509**(12), 4394–4398 (2011)
13. I. Bsoul, S. Mahmood, Magnetic and structural properties of $BaFe_{12-x}Ga_xO_{19}$ nanoparticles. J. Alloy. Compd. **489**(1), 110–114 (2010)
14. M.V. Rane et al., Magnetic properties of NiZr substituted barium ferrite. J. Magn. Magn. Mater. **195**(2), L256–L260 (1999)
15. D. Mishra et al., Studies on characterization, microstructures and magnetic properties of nano-size barium hexa-ferrite prepared through a hydrothermal precipitation–calcination route. Mater. Chem. Phys. **86**(1), 132–136 (2004)
16. L. Rezlescu et al., Fine barium hexaferrite powder prepared by the crystallisation of glass. J. Magn. Magn. Mater. **193**(1), 288–290 (1999)
17. X. Liu et al., An ultrafine barium ferrite powder of high coercivity from water-in-oil microemulsion. J. Magn. Magn. Mater. **184**(3), 344–354 (1998)
18. A. Ataie, S. Heshmati-Manesh, Synthesis of ultra-fine particles of strontium hexaferrite by a modified co-precipitation method. J. Eur. Ceram. Soc. **21**(10), 1951–1955 (2001)
19. V. Sankaranarayanan, D. Khan, Mechanism of the formation of nanoscale M-type barium hexaferrite in the citrate precursor method. J. Magn. Magn. Mater. **153**(3), 337–346 (1996)
20. L. Junliang et al., Synthesis and magnetic properties of quasi-single domain M-type barium hexaferrite powders via sol–gel auto-combustion: effects of pH and the ratio of citric acid to metal ions (CA/M). J. Alloy. Compd. **479**(1), 863–869 (2009)
21. P. Meng et al., Tunable complex permeability and enhanced microwave absorption properties of $BaNi_xCo_{1-x}TiFe_{10}O_{19}$. J. Alloy. Compd. **628**, 75–80 (2015)
22. Y. Xu et al., Theory of the single ion magnetocrystalline anisotropy of 3d ions. Phys. Status Solidi B **157**(2), 685–693 (1990)
23. A.K. Singh et al., Dielectric properties of Mn-substituted Ni–Zn ferrites. J. Appl. Phys. **91**(10), 6626–6629 (2002)
24. I. Soibam, S. Phanjoubam, L. Radhapiyari, Dielectric properties of Ni substituted Li–Zn ferrites. Phys. B **405**(9), 2181–2184 (2010)
25. V.V. Soman, V. Nanoti, D. Kulkarni, Dielectric and magnetic properties of Mg–Ti substituted barium hexaferrite. Ceram. Int. **39**(5), 5713–5723 (2013)
26. K.S. Moghaddam, A. Ataie, Role of intermediate milling in the processing of nano-size particles of barium hexaferrite via co-precipitation method. J. Alloy. Compd. **426**(1), 415–419 (2006)
27. I. Coondoo et al., Structural, dielectric and impedance spectroscopy studies in $(Bi_{0.90}R_{0.10})Fe_{0.95}Sc_{0.05}O_3$ [R = La, Nd] ceramics. Ceram. Int. **40**(7), 9895–9902 (2014)
28. R.D. Shannon, Revised effective ionic radii and systematic studies of interatomic distances in halides and chalcogenides. Acta Crystallogr. Sect. A **32**(5), 751–767 (1976)
29. P.P. Naik et al., Influence of rare earth (Nd^{+3}) doping on structural and magnetic properties of nanocrystalline manganese-zinc ferrite. Mater. Chem. Phys. **191**, 215–224 (2017)
30. D. Vinnik et al., Growth, structural and magnetic characterization of Co-and Ni-substituted barium hexaferrite single crystals. J. Alloy. Compd. **628**, 480–484 (2015)
31. Y. Xie et al., Synthesis and magnetic properties of $BaFe_{11.92}La_{(0.08-x)}Nd_xO_{19}$ (x = 0, 0.02, 0.04, 0.06, 0.08) via gel-precursor self-propagating combustion process. J. Magn. Magn. Mater. **377**, 172–175 (2015)
32. V.C. Chavan et al., Transformation of hexagonal to mixed spinel crystal structure and magnetic properties of Co^{2+} substituted $BaFe_{12}O_{19}$. J. Magn. Magn. Mater. **398**, 32–37 (2016)
33. I. Ali et al., Effects of Ga–Cr substitution on structural and magnetic properties of hexaferrite ($BaFe_{12}O_{19}$) synthesized by sol–gel auto-combustion route. J. Alloy. Compd. **547**, 118–125 (2013)
34. A. Gonzalez-Angeles et al., Magnetic studies of NiSn-substituted barium hexaferrites processed by attrition milling. J. Magn. Magn. Mater. **270**(1), 77–83 (2004)

35. M.V. Rane et al., Mössbauer and FT-IR studies on non-stoichiometric barium hexaferrites. J. Magn. Magn. Mater. **192**(2), 288–296 (1999)
36. D.A. Vinnik et al., Cu-substituted barium hexaferrite crystal growth and characterization. Ceram. Int. **41**(7), 9172–9176 (2015)
37. Z. Yang et al., (Zn, Ni, Ti) substituted barium ferrite particles with improved temperature coefficient of coercivity. Mater. Sci. Eng. B **90**(1), 142–145 (2002)
38. M.J. Iqbal, M.N. Ashiq, P. Hernandez-Gomez, Effect of annealing temperature and substitution of Zr–Cu on magnetic properties of strontium hexaferrite nanoparticles. *Journal of Physics: Conference Series* (IOP Publishing, Bristol, 2009)
39. M.A. Rafiq, M.N. Rafiq, K.V. Saravanan, Dielectric and impedance spectroscopic studies of lead-free barium-calcium-zirconium-titanium oxide ceramics. Ceram. Int. **41**(9), 11436–11444 (2015)
40. M.A. Rafiq et al., Defects and charge transport in Mn-doped $K_{0.5}Na_{0.5}NbO_3$ ceramics. Phys. Chem. Chem. Phys. **17**(37), 24403–24411 (2015)
41. A. Kamal et al., Structural and impedance spectroscopic studies of CuO-doped ($K_{0.5}Na_{0.5}Nb_{0.995}Mn_{0.005}O_3$) lead-free piezoelectric ceramics. Appl. Phys. A **122**, 1037 (2016)
42. M.A. Rafiq et al., Impedance analysis and conduction mechanisms of lead free potassium sodium niobate (KNN) single crystals and polycrystals: a comparison study. Cryst. Growth Des. **15**(3), 1289–1294 (2015)
43. V.V. Soman et al., Effect of Substitution of Zn–Ti on magnetic and dielectric properties of $BaFe_{12}O_{19}$. Phys. Proc. **54**, 30–37 (2014)
44. N. Ponpandian, P. Balaya, A. Narayanasamy, Electrical conductivity and dielectric behaviour of nanocrystalline $NiFe_2O_4$ spinel. J. Phys.: Condens. Matter. **14**(12), 3221 (2002)
45. R. Pattanayak et al., Electric transport properties study of bulk $BaFe_{12}O_{19}$ by complex impedance spectroscopy. Phys. B **474**, 57–63 (2015)
46. J.R. Macdonald, W.B. Johnson, Fundamentals of impedance spectroscopy. *Impedance Spectroscopy: Theory, Experiment, and Applications*, 2nd edn. (Wiley, Hoboken, 2005), pp. 1–26
47. Q.K. Muhammad et al., Structural, dielectric, and impedance study of ZnO-doped barium zirconium titanate (BZT) ceramics. J. Mater. Sci. **51**(22), 10048–10058 (2016)
48. O. Raymond et al., Frequency-temperature response of ferroelectromagnetic $Pb(Fe_{1/2}Nb_{1/2})O_3$ ceramics obtained by different precursors. Part II. Impedance spectroscopy characterization. J. Appl. Phys. **97**(8), 084108 (2005)